Available online at www.sciencedirect.com

ScienceDirect

Physics Procedia 64 (2015) 19 – 27

Physics Procedia

Scientific Workshop on Nuclear Fission Dynamics and the Emission of Prompt Neutrons and Gamma Rays, THEORY-3

Inclusion of angular momentum in FREYA

Jørgen Randrup[a,*], Ramona Vogt[b,c]

[a]*Nuclear Science Division, Lawrence Berkeley National Laboratory, Berkeley, California 94720, USA*
[b]*Physics Division, Lawrence Livermore National Laboratory, Livermore, California 94551, USA*
[c]*Physics Department, University of California, Davis, California 95616, USA*

Abstract

The event-by-event fission model FREYA generates large samples of complete fission events from which any observable can extracted, including fluctuations of the observables and the correlations between them. We describe here how FREYA was recently refined to include angular momentum throughout. Subsequently we present some recent results for both neutron and photon observables.

Peer-review under responsibility of the European Commission, Joint Research Centre – Institute for Reference Materials and Measurements

Keywords: Fission modeling; prompt neutrons; prompt photons; angular momentum; fluctuations; correlations; Monte Carlo simulation.

1. Introduction

FREYA (Fission Reaction Event Yield Algorithm) was developed to produce large samples of complete fission events from which any desired fission observable can subsequently be extracted [Randrup and Vogt (2009)]. Each fission event is characterized by full information about the two product nuclei and the emitted neturons and photons:

$$A_{\rm L},\ Z_{\rm L},\ \boldsymbol{P}_{\rm L},\ \boldsymbol{S}_{\rm L} \quad : \text{mass \& charge number and linear \& angular momentum of the light product nucleus,} \tag{1}$$
$$A_{\rm H},\ Z_{\rm H},\ \boldsymbol{P}_{\rm H},\ \boldsymbol{S}_{\rm H} \quad : \text{mass \& charge number and linear \& angular momentum of the heavy product nucleus,} \tag{2}$$
$$\boldsymbol{p}_n,\ n=1,\ldots,\nu \quad : \text{momenta of the } \nu \text{ neutrons,} \tag{3}$$
$$\boldsymbol{q}_m,\ m=1,\ldots,N_\gamma \quad : \text{momenta of the } N_\gamma \text{ photons.} \tag{4}$$

It is straightforward to obtain any observable, including fluctuations and correlations, and detection cuts and acceptances can readily be incorporated. Furthermore, because the event generation is very fast, it is practical to incorporate FREYA into existing transport codes.

* Corresponding author. Tel.: +1-510-486-6157; fax: +1-510-486-4794.
E-mail address: JRandrup@LBL.gov

Peer-review under responsibility of the European Commission, Joint Research Centre – Institute for Reference Materials and Measurements
doi:10.1016/j.phpro.2015.04.003

2. FREYA without angular momentum

To facilitate the later discussion, we first describe how FREYA works without consideration of angular momentum. More complete descriptions have been given by Randrup and Vogt (2009); Vogt *et al.* (2009, 2011, 2012); Vogt and Randrup (2013); Randrup and Vogt (2014).

The excitation energy of the initial fissionable nucleus is determined from the energy of the incoming neutron, or specified explicitly (as is useful when addressing photon-induced fission leading to excitations below the neutron separation energy). Sequential pre-fission evaporation is considered in competition with fission according to a simple model for Γ_n/Γ_f [Vogt *et al.* (2012)].

Once the mass number A_0, charge number Z_0, and excitation energy E_0 of the fissioning nucleus have been determined, the first task is to select the mass partition, *i.e.* the mass numbers of the two primary fission fragments, A_L and A_H. This is done by sampling one of them from a specified mass distribution based on experimental data and then obtaining the other one by baryon number conservation, $A_L + A_H = A_0$. Subsequently, the fragment charge numbers Z_L and Z_H are obtained by sampling one of them from a distribution of the form $P(Z_i; A_i) \sim \exp(-(Z_i - \overline{Z}_i)^2/2\sigma_Z^2)$ with $\overline{Z}_i = (Z_0/A_0)A_i$, as suggested by experiment [Reisdorf *et al.* (1971); Lemaire *et al.* (2005)] and then getting the other one by charge conservation, $Z_L + Z_H = Z_0$.

The fragments are emitted back-to-back in the frame of the fissioning nucleus and their total kinetic energy TKE is determined in several steps. For the given mass split, the average value of the total kinetic energy is taken as $\overline{\mathrm{TKE}}(A_f) = \mathrm{TKE}_{\mathrm{exp}}(A_f) - d\mathrm{TKE}(E_0)$, where the (relatively small) shift away from the data is adjusted so that the resulting overall mean neutron multiplicity $\bar{\nu}$ matches the experimental value at the given energy E_0. The mean total fragment energy of the two fragments, $\overline{E}^*$, then follows from energy conservation,

$$\overline{E}^* = \overline{E}^*_L + \overline{E}^*_H = Q_{LH} + E_0 - \overline{\mathrm{TKE}}\,. \tag{5}$$

Here $Q_{LH} = M(A_0, Z_0) - M(A_L, Z_L) - M(A_H, Z_H)$ is the Q-value for the particular mass-charge split. In thermal equilibrium the mean excitations of the individual fragments are in proportion to their respective heat capacities, which, in the simple Fermi-gas model, in turn are proportional to the level-density parameters $a_i = A_i/e_0$, where $e_0 \approx 10\,\mathrm{MeV}$ is taken as a somewhat adjustable parameter. The corresponding common temperature T is given by $\overline{E}^* = (a_L + a_H)T^2$. But because the light fragment tends to acquire more than its "fair share" of the excitation, we adjust these averages by means of the adjustable parameter x, taking the individual fragment excitations to be

$$\overline{E}^*_L = x\,\frac{a_L}{a_L + a_H}\,\overline{E}^*\,,\quad \overline{E}^*_H = \overline{E}^* - \overline{E}^*_L\,. \tag{6}$$

Subsequently we sample the fluctuations in excitation, δE^*_L and δE^*_H, using that the equilibrium variance in E^*_i is given by $\sigma^2(E^*_i) = 2\overline{E}^*_i T$ and we thus obtain the actual fragment excitations as $E^*_i = \overline{E}^*_i + \delta E^*_i$. The total kinetic energy is then adjusted correspondingly,

$$\mathrm{TKE} = \overline{\mathrm{TKE}} - \delta E^*_L - \delta E^*_H\,. \tag{7}$$

The direction of the relative fragment motion is sampled isotropically and the individual fragment momenta $\boldsymbol{P}_L$ and $\boldsymbol{P}_H$ then follow by energy and momentum conservation.

The fully accelerated fragments undergo sequential neutron evaporation as long as it is energetically possible and the resulting product nuclei subsequently dispose of their excitation by sequential emission of photons. At each step for both processes, the maximum possible temperature in the daughter nucleus is calculated, T_{max}, and the kinetic energy of the ejectile is then sampled from a simple black-body spectral profile. The non-relativistic form is used for neutrons while the ultra-relativistic form is used for photons,

$$dN_n/d\epsilon_n \sim \epsilon_n \exp(-\epsilon_n/T_{\mathrm{max}})\,,\quad dN_\gamma/d\epsilon_\gamma \sim \epsilon_\gamma^2 \exp(-\epsilon_\gamma/T_{\mathrm{max}})\,, \tag{8}$$

where the kinetic energies are $\epsilon_n = |\boldsymbol{p}_n|^2/2m$ for the ν neutrons and $\epsilon_m = |\boldsymbol{q}_m|$ for the N_γ photons. All ejectiles are emitted isotropically in the respective emitter frame and the nuclear momentum recoils are taken into account after each individual emission.

It is possible to generate one million complete fission events in about ten seconds on a standard laptop computer.

3. Incorporation of angular momentum

Angular momentum in FREYA is taken into account at three distinct stages: prior to fission, at scission, and during the sequential decay of the fission fragments.

3.1. Pre-scission angular momentum

The angular momentum of the initial compound nucleus is either specified explicitly or obtained by sampling the impact parameter of the incoming neutron, assuming that it is fully absorbed. The effect of rotation on the possible pre-fission sequential neutron evaporation is treated in the same manner as the evaporation from the rotating fission fragments. The resulting pre-fission angular momentum is denoted by $\boldsymbol{S}_0$.

3.2. Scission

At scission each of the two fragments will inherit its share of $\boldsymbol{S}_0$. The mean fragment spins will then be $\overline{\boldsymbol{S}}_i = (\mathcal{I}_i/\mathcal{I})\boldsymbol{S}_0$, where $\mathcal{I} = \mathcal{I}_\mathrm{L} + \mathcal{I}_\mathrm{H} + \mathcal{I}_\mathrm{R}$ is the total moment of inertia and $\mathcal{I}_\mathrm{R} = \mu R^2$ where $\boldsymbol{R} = \boldsymbol{R}_\mathrm{L} - \boldsymbol{R}_\mathrm{H}$. The remainder of $\boldsymbol{S}_0$ will become the mean angular momentum of the relative fragment motion, $\boldsymbol{L} = \mu\boldsymbol{R}\times\boldsymbol{U} = (\mathcal{I}_\mathrm{R}/\mathcal{I})\boldsymbol{S}_0$, where $\boldsymbol{U} = \dot{\boldsymbol{R}}_\mathrm{L} - \dot{\boldsymbol{R}}_\mathrm{H}$ is the relative fragment velocity right after scission.

In addition to the above average fragment spins arising from the overall rotation of the dinuclear complex, the two fragments also acquire fluctuating amounts, $\delta\boldsymbol{S}_L$ and $\delta\boldsymbol{S}_H$. Generally, a dinuclear system has six normal modes of rotation [Døssing and Randrup (1985)], namely *tilting* and *twisting*, in which the fragments rotate in the same or in the opposite sense around the dinuclear axis $\hat{\boldsymbol{z}} = \boldsymbol{R}/R$, and *wriggling* and *bending*, in which the fragments rotate in the same or in the opposite sense around an axis perpendicular to the dinuclear axis, see Fig. 1. The two latter types of mode are then each doubly degenerate, corresponding to independent rotations around $\hat{\boldsymbol{x}}$ and $\hat{\boldsymbol{y}}$. As in Vogt and Randrup (2013), we consider only the latter four modes because the agitation of the former two tends to be suppressed due to the constricted neck [Døssing and Randrup (1985)].

The contribution to the rotational energy from these four dinuclear rotational modes is given by

$$\delta E_\mathrm{rot} = \boldsymbol{s}_+^2/2\mathcal{I}_+ + \boldsymbol{s}_-^2/2\mathcal{I}_- \,, \tag{9}$$

where the angular momenta of the normal modes have the form $\boldsymbol{s}_\pm = (s_\pm^x, s_\pm^y, 0)$, with the plus referring to the wriggling modes (in which the rotations of the two fragments are parallel) and the minus to the bending modes (in which the rotations of the two fragments are opposite). The associated moments of inertia are

$$\mathcal{I}_+ = (\mathcal{I}_\mathrm{L} + \mathcal{I}_\mathrm{H})\mathcal{I}/\mathcal{I}_R \,, \quad \mathcal{I}_- = \mathcal{I}_\mathrm{L}\mathcal{I}_\mathrm{H}/(\mathcal{I}_\mathrm{L} + \mathcal{I}_\mathrm{H}) \,. \tag{10}$$

It is assumed that these normal dinuclear rotational modes are being agitated statistically during the scission process. Thus, in each event, the values of $\boldsymbol{s}_\pm$ are being sampled from distributions of the form

$$P_\pm(\boldsymbol{s}_\pm = (s_\pm^x, s_\pm^y, 0))\, ds_\pm^x ds_\pm^y \sim \mathrm{e}^{-s_\pm^2/2\mathcal{I}_\pm T_S}\, ds_\pm^x ds_\pm^y, \tag{11}$$

where the "spin temperature" is related to the scission temperature by $T_S = c_S T$, with c_S taken as a somewhat adjustable global parameter.

Other recent Monte Carlo calculations of prompt photon emission from fission fragments [Litaize (2010); Regnier (2012); Becker (2013)] do not keep track of the fragment spin directions but consider only their magnitudes. Integer values of these, J_i, are sampled independently for each fragment from distributions of the form $P(J_i) \sim (2J_i+1)\exp(J_i(J_i+1)/2\sigma^2)$ [Becker (2013)] or $P(J_i) \sim (2J_i+1)\exp((J_i+\frac{1}{2})^2/2\sigma^2)$ [Litaize (2010); Regnier (2012)] where the spin cut-off parameter σ is either [Litaize (2010)] specified ($\sqrt{2}\sigma = 6\hbar$ for light fragments and $\sqrt{2}\sigma = 7.2\hbar$ for heavy fragments) or [Regnier (2012); Becker (2013)] taken from the RIPL3.0 data library [RIPL (2009)].

In FREYA the fluctuating angular momentum components of the individual fragments are given by

$$\delta S_\mathrm{L}^{x,y} = (\mathcal{I}_\mathrm{L}/\mathcal{I}_+)s_+^{x,y} + s_-^{x,y} \,, \quad \delta S_\mathrm{H}^{x,y} = (\mathcal{I}_\mathrm{H}/\mathcal{I}_+)s_+^{x,y} - s_-^{x,y} \,, \quad \delta S_\mathrm{L}^z = \delta S_\mathrm{H}^z = 0 \,. \tag{12}$$

Consequently, the total angular momenta of the fragments are $\boldsymbol{S}_\mathrm{L} = \overline{\boldsymbol{S}}_\mathrm{L} + \delta\boldsymbol{S}_\mathrm{L}$ and $\boldsymbol{S}_\mathrm{H} = \overline{\boldsymbol{S}}_\mathrm{H} + \delta\boldsymbol{S}_\mathrm{H}$.

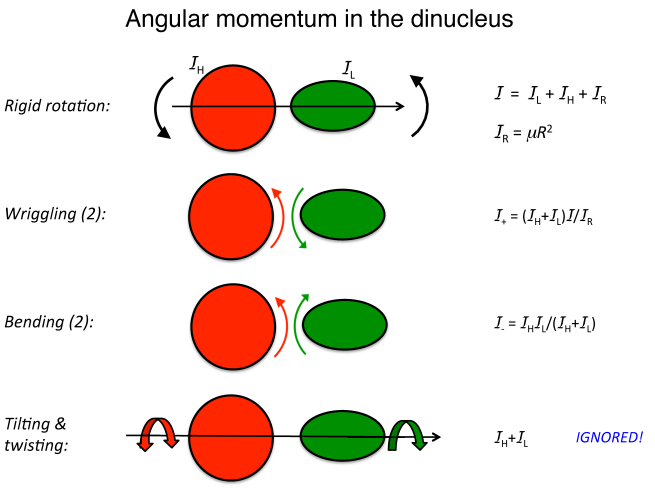

Fig. 1. Angular momentum is included in FREYA by augmenting the rigidly rotating scission configuration (*top*) by the (doubly degenerate) dinuclear wriggling and bending modes, for which the fragment rotations are perpendicular to the dinuclear axis, while ignoring the tilting and twisting modes (*bottom*), for which the rotations are directed along the dinuclear axis.

The resulting orbital angular momentum is then $\boldsymbol{L} = \overline{\boldsymbol{L}} - \delta\boldsymbol{S}_{\rm L} - \delta\boldsymbol{S}_{\rm H}$. Because the geometrical configuration has not been affected by the angular-momentum fluctuations, the "exit" z axis remains the same, $\hat{\boldsymbol{z}}' = \hat{\boldsymbol{z}} = \boldsymbol{R}/R$. However, the exit y axis, being directed along the resulting orbital angular momentum, has changed, $\hat{\boldsymbol{y}}' = \boldsymbol{L}/L$, and therefore $\hat{\boldsymbol{x}}' = \hat{\boldsymbol{y}}' \times \hat{\boldsymbol{z}}'$ also differs from $\hat{\boldsymbol{x}}$.

The fragment rotations reduce the scission excitation energy, so (5) is modified,

$$\overline{E}^* = \overline{E}^*_{\rm L} + \overline{E}^*_{\rm H} = Q_{\rm LH} + E_0 - \overline{\rm TKE} - S^2_{\rm L}/2\mathcal{I}_{\rm L} - S^2_{\rm H}/2\mathcal{I}_{\rm H}\,. \tag{13}$$

3.3. Exit trajectory

Because the further relative fragment motion is subject to the dinuclear Coulomb force, the asymptotic fragment motion is not along the direction of the dinuclear scission axis. We estimate the resulting final direction by assuming that the separating fragments follow a Coulomb trajectory with the scission configuration being the closest approach, an approximation that ignores the initial radial kinetic energy (which is quite small compared to the nearly 200 MeV gained from the Coulomb push). The resulting effect is typically just a few degrees.

4. Neutron evaporation with angular momentum

The original FREYA evaporation procedure has been modified in two regards to take account of angular momentum: 1) the emitting nucleus may generally be rotating, and 2) the emitted neutron carries away some angular momentum. The general approach is as follows: First the emission point is selected randomly on the nuclear surface and a neutron is then emitted from the local surface element as usual, but it is subsequently boosted by the local rotational velocity of the emission point and the linear and angular momentum recoils are taken into account.

Because these effects are relatively small, it is assumed for simplicity that the evaporating nuclei are spherical. Then the orientation of the shape is unaffected by the nuclear rotation and the formulas are simpler. The treatment below holds in the center-of-mass (CM) system of the evaporating nucleus. The nuclear CM reference system xyz is aligned with the adopted external XYZ reference system, its origin is at the CM of the emitting nucleus, and it is moving with the CM velocity. In this coordinate system, the points (x, y, z) located on the spherical surface of the emitting nucleus are characterized by $x^2 + y^2 + z^2 = R_A^2$, where $R_A = r_0 A^{1/3}$ is the nuclear radius. It is therefore

straightforward to sample the emission point $\boldsymbol{r} = (x, y, z) = R_A(\sin\vartheta\cos\varphi, \sin\vartheta\sin\varphi, \cos\vartheta)$. The nuclear rotation vector is $\boldsymbol{\omega} = \boldsymbol{S}/\mathcal{I}$, so the local rotational velocity $\boldsymbol{w}$ at the emission point $\boldsymbol{r}$ is given by $\boldsymbol{w}(\boldsymbol{r}) = (w_x.w_y, w_z) = \boldsymbol{\omega} \times \boldsymbol{r}$.

In order to sample the local velocity of the emitted neutron, we need to introduce a local reference system *abc*, where $\hat{\boldsymbol{c}}$ points outwards along the local surface normal (so that the *ab* plane is tangential to the surface at the emission point $\boldsymbol{r}$). Because the shape is a sphere, the local normal is directed along $\boldsymbol{r}$, so $\hat{\boldsymbol{c}} = \boldsymbol{r}/r$. Choosing $\hat{\boldsymbol{b}}$ to lie in the XY plane, we then use

$$\hat{\boldsymbol{a}} = \hat{\boldsymbol{b}} \times \hat{\boldsymbol{c}} = (\cos\vartheta\cos\varphi, \cos\vartheta\sin\varphi, -\sin\vartheta)\,, \tag{14}$$

$$\hat{\boldsymbol{b}} = \hat{\boldsymbol{c}} \times \hat{\boldsymbol{a}} = (-\sin\varphi, \cos\varphi, 0)\,, \tag{15}$$

$$\hat{\boldsymbol{c}} = \hat{\boldsymbol{a}} \times \hat{\boldsymbol{b}} = (\sin\vartheta\cos\varphi, \sin\vartheta\sin\varphi, \cos\vartheta)\,. \tag{16}$$

To sample the emission velocity $\boldsymbol{u}$ in the local co-moving *abc* frame, we first sample the emission energy ϵ as before using $P(\epsilon) \sim \epsilon\exp(-\epsilon/T_{\max})$, and then sample the (outwards) direction (θ, ϕ) (where the polar angle θ is measured relative to the local surface normal $\hat{\boldsymbol{c}}$) from a distribution biased by the normal component $\cos\theta$: $\cos^2\theta = \eta$ and $\phi = 2\pi\eta'$ (where η and η' are random numbers uniform on $(0, 1]$), so that

$$\boldsymbol{u} = u\sin\theta\cos\phi\,\hat{\boldsymbol{a}} + u\sin\theta\sin\phi\,\hat{\boldsymbol{b}} + u\cos\theta\,\hat{\boldsymbol{c}}\,. \tag{17}$$

Because the sampled energy ϵ is the kinetic energy of the relative motion of the emitted neutron and the residual daughter nucleus, we have (non-relativistically) $\epsilon = \frac{1}{2}\mu u^2$ where μ is the reduced mass, $1/\mu = 1/m + 1/M'$. The local velocity of the emitted neutron is therefore $\boldsymbol{u}_{\rm n}) = \boldsymbol{u}/(1 + m/M')$ and its total velocity in the CM of the emitting nucleus is $\boldsymbol{v}_{\rm n} = \boldsymbol{u}_{\rm n} + \boldsymbol{w}$, where $\boldsymbol{w}$ is the local boost from the rotation. Its momentum is then $\boldsymbol{p}_{\rm n} = m\boldsymbol{v}_{\rm n}$ and momentum conservation dictates that the momentum of the daughter nucleus be $\boldsymbol{P}' = -\boldsymbol{p}_{\rm n}$, in the CM of the mother nucleus.

Furthermore, by angular-momentum conservation we may obtain the angular momentum of the daughter nucleus, $\boldsymbol{S}' = \boldsymbol{S} - \boldsymbol{\ell}$, where $\boldsymbol{\ell} = \boldsymbol{r} \times \boldsymbol{p}_{\rm n}$ is the angular momentum carried away by the emitted neutron. The corresponding rotational energy of the residue is $E'_{\rm rot} = (S')^2/2\mathcal{I}'$. The energy balance then determines Q', the statistical excitation energy of the daughter,

$$Q' = Q - S_{\rm n} - \epsilon + E_{\rm rot} - E'_{\rm rot}\,, \tag{18}$$

where Q is the statistical excitation of the mother nucleus and $E_{\rm rot} = S^2/2\mathcal{I}$ is its rotational energy, and the neutron separation energy is $S_{\rm n} = M' + m - M$.

The Q-value for neutron evaporation, $Q^*_{\rm n}$, is equal to the maximum possible statistical excitation in the daughter nucleus, $Q'_{\max}$. Without angular momentum taken into account, the softest emission has $\epsilon = 0$ and leads to the maximal excitation energy in the daughter. However, when angular momentum is incorporated, even such an ultra-soft emission generally produces both linear and angular recoils due to the rotational motion of the emission point. Only when the emission point $\boldsymbol{r}$ is at one of the poles (*i.e.*, $\boldsymbol{r}$ is along or opposite the angular momentum $\boldsymbol{S}$), then there is no rotational motion $\boldsymbol{w}$ and an ultra-soft emission produces no recoil, (*i.e.*, the linear and angular momenta of the daughter nucleus then remain the same as those of the mother). Because the daughter nucleus has a smaller moment of inertia, it will have a larger rotational energy. As a consequence, Q^*_n is correspondingly reduced,

$$Q^*_n = M + S^2/2\mathcal{I} + Q - m_n - M' - S^2/2\mathcal{I}'\,. \tag{19}$$

Furthermore, as before, it is necessary to verify that a given sampled emission energy ϵ does not violate the bound set by energy conservation (*i.e.*, the resulting statistical excitation Q' must be positive). The inclusion of the rotational motion introduces stricter bounds that depend on the location of the emission point $\boldsymbol{r}$. Therefore a given sampling of ϵ must be repeated more frequently, though still relatively rarely.

5. Photon emission

After neutron evaporation has ceased, the residual product nucleus has a statistical excitation energy of $Q < S_{\rm n}$. It now proceeds to deexcite by sequential photon emission which is assumed to occur in two stages: First the statistical excitation energy is radiated away by sequential photon emission, leaving a cold but rotating product nucleus, which then completes its deexcitation by photon emission along the yrast line.

The statistical photon emission is treated in a manner analogous to neutron evaporation, see Eq. (8), the only differences being that the photon has no mass and no separation energy (so an infrared cut-off is introduced). The procedure for statistical emission is repeated until the available statistical excitation energy has been exhausted. The remaining excitation is then purely rotational and is disposed of by a stretched E2 cascade, in which each photon reduces the product spin by two units.

6. Illustrative results

The most important rotational effects in fission at low energy arise from the angular momenta of the fragments, primarily acquired at scission. To bring these effects out as clearly as possible, we consider here spontaneous fission where there is no rotation prior to scission nor any pre-fission neutrons emitted.

Table 1 shows how much angular momentum the fragments acquire in various scenarios. In scenario 0 the primary fission fragments are not endowed with any angular momentum fluctuations and, because we are considering spontaneous fission, the average fragment angular momenta also vanish initially and their final angular momenta (prior to the photon deexcitation) are due solely to the evaporation recoils.

Table 1. The three scenarios considered for spontaneous fission of ^{252}Cf which are distinguished by the value of the factor $c_S = T_S/T_{sc}$ that governs the magnitude of the fragment spin fluctuations. For each scenario are the values of the usual FREYA parameters e_0, x and dTKE (in MeV), the latter having been adjusted so that the resulting average neutron multiplicity $\bar{\nu}$ is approximately the same for all scenarios. Also shown are the resulting mean magnitudes of the angular momenta of the initial light and heavy fission fragments, $\overline{S}_L$ and $\overline{S}_H$. [From Randrup and Vogt (2014).]

^{252}Cf(sf)	e_0	x	dTKE	$\bar{\nu}$	$\overline{S}_L$ ($\hbar$)	$\overline{S}_H$ ($\hbar$)
0: c_S=0.0	10	1.3	2.6	3.76	0.02	0.02
1: c_S=0.1	10	1.3	2.4	3.76	1.82	2.25
2: c_S=1.0	10	1.3	0.5	3.75	6.16	7.63

One would expect that the angular distribution of neutrons evaporated from a rotating nucleus will acquire an oblate shape due to the rotational boost that enhances emission in the plane perpendicular to the angular momentum $\boldsymbol{S}$ of the emitting nucleus. This is illustrated in Fig. 2 (*left*), which shows, in the three scenarios, the angular distribution of the evaporated neutrons relative to the spin direction of the emitting nucleus. There is indeed a preference for equatorial emission which increases steadily with c_S, but the flattening never exceeds a rather modest level. The effect for scenario 0, in which the fragments are formed without any rotation, is due to sequential neutron emission: After the first neutron emission, a fragment will generally rotate somewhat as a result of the recoil, so subsequent neutron emissions generally occur from nuclei that rotate and they will therefore be subject to the associated centrifugal force.

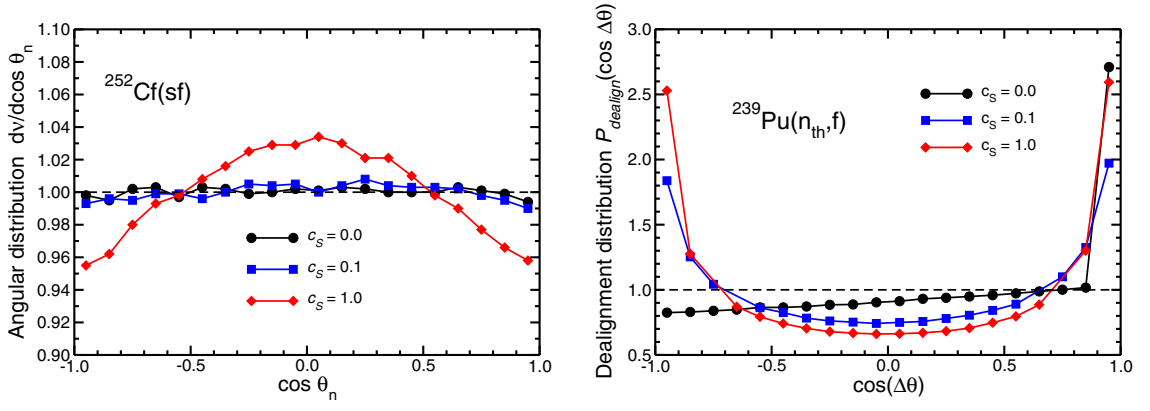

Fig. 2. *Left:* The angular distribution of evaporated neutrons relative to the direction of the angular momentum of the emitting nucleus, as obtained for ^{252}Cf(sf) in the three scenarios. *Right:* The distribution of the angle between the post-evaporation fragment angular momentum and that of the initial compound nucleus, $\Delta\theta$, for $c_S = 0, 0.1, 1.0$, with dTKE having been adjusted in each scenario to yield $\bar{\nu} = 2.75$. [Randrup and Vogt (2014)]

In order to illustrate the angular momentum effects for fission of initially rotating nuclei, we consider thermal-neutron induced fission, namely ^{239}Pu(n$_{\rm th}$,f). The absorption of the incoming neutron endows the resulting compound nucleus, ^{240}Pu, with a (small) angular momentum $\boldsymbol{S}_0$. Thus the scission configuration is (slowly) rotating and, as a consequence, the nascent fission fragments have a nonvanishing (though small) average angular momentum component directed along $\boldsymbol{S}_0$, in addition to the fluctuating amounts acquired during scission. Subsequently, the fragment angular momenta are modified slightly by each neutron evaporation. Figure 2 (*right*) shows the directional correlation between the post-evaporation fragment angular momenta $\boldsymbol{S}'_i$ and the initial compound angular momentum $\boldsymbol{S}_0$.

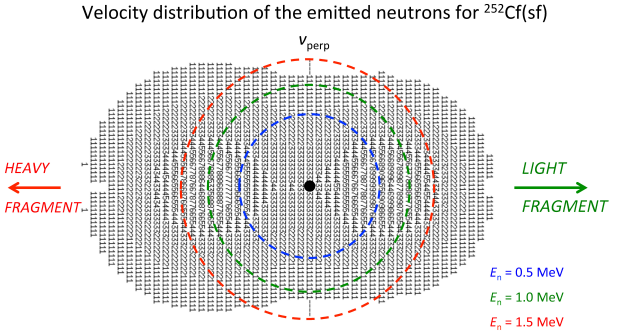

Fig. 3. A cut through the three-dimensional distribution of the neutron velocities. The circles correspond to the specified values of the neutron kinetic energy in the laboratory pppppppp($E_{\rm n}$ = 0.5, 1.0, 1.5 MeV) which is indicated by the dot. Such a contour plot was preented in Bowman *et al.* (1963).

Because the neutrons are evaporated from fragments that are moving oppositely, their angular distribution is not isotropic and they have non trivial angular correlations. The kinematical situation is illustrated in Fig. 3. The dumbbell shape the neutron distribution is reflected in the angular distribution of the neutrons relative to the fragment direction, as illustrated in Fig. 4 (*left*). The calculated results compare well with those obtained from experiment Fig. 4 (*right*).

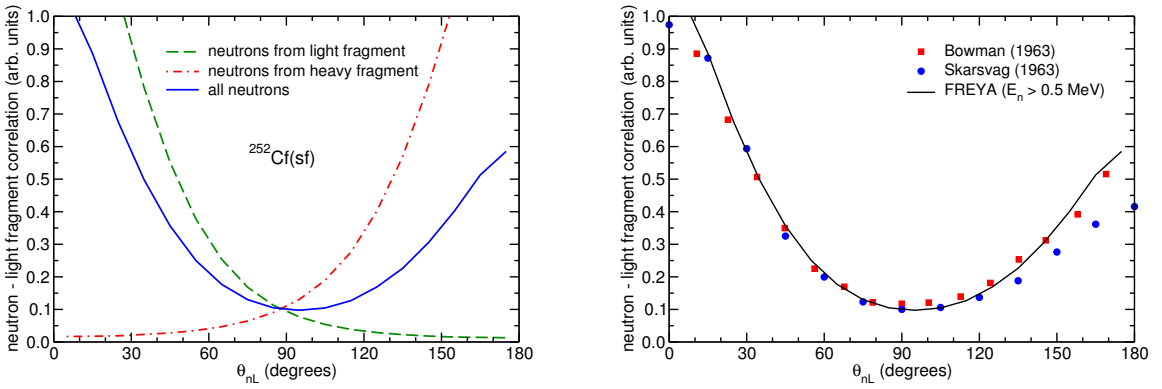

Fig. 4. *Left:* The default `FREYA` calculations are shown for ^{252}Cf(sf) neutrons correlated with the light fragment. The neutrons emitted from the light fragment (dashed red) and those emitted from the heavy fragment (dot-dot-dashed blue) are compared to the correlation of all neutrons with the light fragment; all neutrons have a minimum kinetic energy of 0.5 MeV. *Right:* The default `FREYA` calculations are compared to ^{252}Cf(sf) neutron-light fragment angular correlation data [Bowman *et al.* (1963)] (red squares) and [Skarsvag and Bergheim (1963)] (blue circles); the minimum kinetic energy of the neutrons is 0.5 MeV. [From Vogt and Randrup (2014).]

The neutron-neutron angular correlation is of particular interest and we therefore illustrate (in Fig. 5) the robustness of this observable by changing the model parameters one at a time away from their standard value:

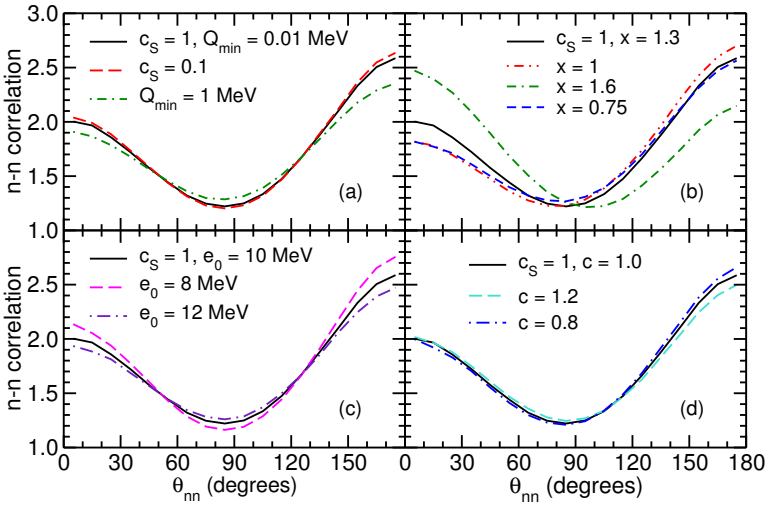

Fig. 5. The angular correlation between two neutrons emitted from ^{252}Cf(sf) as a function of the opening angle between the two neutrons, $\theta_{\rm nn}$. The FREYA results are shown for neutron kinetic energies $E > 0.5$ MeV. The results of different parameter choices in FREYA are compared to the default results: $c_S = 1$, $Q_{\rm min} = 0.01$ MeV, $x = 1.3$, $e_0 = 10$ MeV, and $c = 1$. (a) Parameters affecting photon emission are varied. The dashed red curve is with $c_S = 0.1$, $Q_{\rm min} = 0.01$ MeV while the dot-dashed green curve is with $c_S = 1$, $Q_{\rm min} = 1$ MeV. (b) The parameter affecting the relative excitation energy of the light fragment, x, is varied. The dot-dot-dashed red curve is the result for $x = 1$, equal partition between the light and heavy fragments. T he dot-dashed-dashed green curve shows the result when giving the light fragment even more energy, $x = 1.6$, while the dashed blue curve shows a result with $x = 0.75$, with more excitation given to the heavy than to the light fragment. (c) The parameter governing the level density is varied. The dashed magenta curve is with $e_0 = 8$ MeV while the dot-dashed maroon curve is with $e_0 = 12$ MeV. (d) The parameter governing thermal fluctuations is varied with $c = 1.2$ (dashed turquoise curve) increasing the width of the fluctuation while $c = 0.8$ (dot-dashed blue) decreases it. [From Vogt and Randrup (2014).]

The most striking effect on the shape of the neutron-neutron angular correlation occurs in response to changing the partition of the excitation energy between the light and heavy fragments. The small-angle enhancement for neutrons coming from the same fragment is larger for those emitted by the light fragment because of its higher velocity from the Coulomb repulsion at scission. Furthermore, the relative magnitude of the small-angle and large-angle enhancements evolves as the energy sharing is changed, due to the change in the origin of the emitted neutrons. Thus, for $x = 1.6$ when the light fragment has a large excess energy, the peak at $\theta_{\rm nn} = 0°$ is higher than the peak at $\theta_{\rm nn} = 180°$. The angular correlation function then tilts steadily in favor of the 180° peak as x is decreased. Such large changes in x can be ruled out by comparison to $\nu(A)$ [Vogt and Randrup (2014)].

A recent measurement by Gagarski *et al.* [Gagarski (2008)] was published in 2008. They used a similar setup of two neutron detectors with varying angular separation around the ^{252}Cf source. The detectors were stilbene crystals with photomultiplier tubes surrounded by shielding and the neutrons were separated from photons on the basis of time-of-flight. It was shown that separation between neutrons and photons could be achieved with the photomultiplier tubes down to the detector threshold. By change of the event selection boundaries, it was possible to employ several different neutron detection thresholds: 0.425, 0.55, 0.75, 0.8, 1.2 and 1.6 MeV [Gagarski (2008)]. In Fig. 6 (*left*), our results are compared to the data by Gagarski *et al.* for their various energy thresholds. We again see that the agreement between the calculation and the data is very good for $\theta_{\rm nn} < 90°$, while the calculation overestimates the back-to-back peak for neutrons with kinetic energies less than 1 MeV. The improvement of the agreement between calculations and data at higher neutron energy thresholds suggests that the dependence of the correlation on neutron-photon competition near the evaporation threshold diminishes with neutron energy.

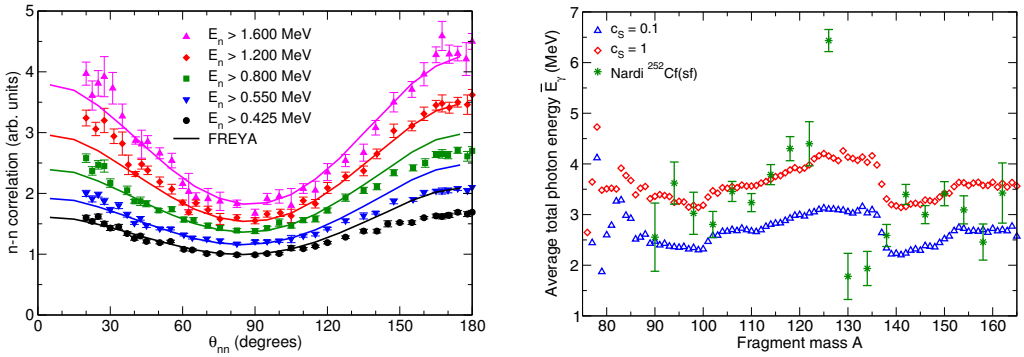

Fig. 6. *Left:* The default FREYA calculations are compared to ^{252}Cf(sf) two-neutron angular correlation data from Gagarski (2008) for neutron kinetic energies greater than 0.425, 0.55, 0.8, 1.2 and 1.6 MeV. *Right:* The average total photon energy as a function of fragment mass A; results calculated for either small ($c_S = 0.1$) or full ($c_S = 1.0$) spin fluctuations are compared to data from Nardi (1973).

We have compared the FREYA results to the measured mass dependence of the average total photon energy released in ^{252}Cf(sf). The small values of c_S that lead to agreement with the recent measurements of the average photon multiplicity N_γ [Chyzh *et al.* (2012); Billnert (2013)], namely $c_S \sim 0.1$ which lead to very low average fragment angular momenta, do not yield good agreement with the earlier measurements of the average total photon energy emitted; agreement with the total photon energy requires $c_S \sim 1$, which also leads to reasonable fragment angular momenta. This is illustrated in Fig. 6 which compares the FREYA results to the Nardi data [Nardi (1973)]. There is a sharp drop in the measured average photon energy at symmetry, A=126, that is not reproduced by the calculations. But apart from the region near symmetry, the trend of the data is reasonably well reproduced with $c_S = 1$.

Acknowledgements

This work was performed under the auspices of the US Department of Energy under Contracts No. DE-AC02-05CH11231 (J.R.) and No. DE-AC52-07NA27344 (R.V.) and it was also supported by the US Department of Energy National Nuclear Security Administration Office of Nonproliferation and Verification Research and Development.

References

Becker, B., Talou, P., Kawano, T., Danon, Y., Stetcu, I., 2013. Phys. Rev. C 87, 014617.
Billnert, R., Hambsch, F.-J., Oberstedt, A., Oberstedt, S., 2013. Phys. Rev. C 87, 024601.
Bowman, H.R., Milton, J.C.D., Thompson, S.G., Swiatecki, W.J., 1963. Phys. Rev. 126, 2120 (1962); Phys. Rev. 129, 2133.
Chyzh, A., et al., 2012. Phys. Rev. C 85, 021601(R).
Døssing, T., Randrup, J., 1985. Nucl. Phys. A 433, 215.
Gagarski, A.M. *et al.*, 2008. Bull. Russ. Acad. Sciences: Physics, 72, 773.
Lemaire, S., Talou, P., Kawano, T., Chadwick, M.B., Madland, D.G., 2005. Phys. Rev. C 72, 024601.
Litaize, O., Serot, O., 2010. Phys. Rev. C 82, 054616.
Nardi, E., Gavron, A., Fraenkel, Z., 1973. Phys. Rev. C 8, 2293.
Randrup, J., Vogt, R., 2009. Phys. Rev. C 80, 024601.
Randrup, J., Vogt, R., 2014. Phys. Rev. C 89, 044601.
Regnier, D., Litaize, O., Serot, O., 2012. Phys. Procedia 31, 59.
Reisdorf, W., Unik, J.P., Griffin, H.C., Glendenin, L.E., 1971. Nucl. Phys. A 177, 337.
Capote, R. et al., 2009. Nucl. Data Sheets 110, 3107.
Skarsvag, K., Bergheim, K., 1963. Nucl. Phys. 45, 72.
Vogt, R., Randrup, J., Pruet, J., Younes, W., 2009. Phys. Rev. C 80, 044611.
Vogt, R., Randrup, J., 2011. Phys. Rev. C 84, 044621.
Vogt, R., Randrup, J., Brown, D.A., Descalle, M.A., Ormand, W.E., 2012. Phys. Rev. C 85, 024608.
Vogt, R., Randrup, J., 2013. Phys. Rev. C 87, 044602.
Vogt, R., Randrup, J., 2014. LLNL-JRNL-661864; Phys. Rev. C (in press).